JOURNAL OF MATERIALS SCIENCE 28 (1993) 5229–5236

Microscopic characterization of sol–gel processed cordierite

J. WERCKMANN, P. HUMBERT
I.P.C.M.S. Groupe Surfaces-Interfaces, U.M.R. 46 C.N.R.S., Université Louis Pasteur, 4 rue Blaise Pascal, 67070 Strasbourg, France

C. ESNOUF
I.N.S.A. Groupe GEMPPM, U.R.A. 341 C.N.R.S., Bat. 502, 20 av. Albert Einstein, 69621 Villeurbanne, France

J. C. BROUDIC, S. VILMINOT
I.P.C.M.S. Groupe Matériaux Inorganiques, U.M.R. 46 C.N.R.S., E.H.I.C.S., 1 rue Blaise Pascal, 67008 Strasbourg, France

Different analytical techniques have been used to characterize green and sintered sol–gel processed cordierite on a microscopic scale. The sintered material, although identified macroscopically as α-cordierite, contains many small precipitates of different chemical composition. Larger precipitates, characterized by an increased Mg concentration, result from inhomogeneities in the precursor gel. Smaller precipitates, identified as mullite and spinel, could not be related to gel heterogeneities. The amorphous phase surrounding the cordierite grains and the precipitates is Mg depleted and Si enriched. Neither μ-cordierite nor β-cordierite were observed; slight variations of the α-cordierite lattice parameters are attributed to some local perturbations due to a slight departure from stoichiometry or Si, Al ordering on tiny domains.

1. Introduction

Cordierite ($2MgO{\cdot}2Al_2O_3{\cdot}5SiO_2$) has many attractive physical properties for microelectronic applications; in particular, it has a low dielectric constant and a thermal expansion coefficient close to that of silicon. This ceramic is therefore a good candidate material for microelectronic packages or 3D-interconnection chips. The synthesis of cordierite by the classic method of oxide mixture suffers, however, from sintering at high temperature (1300–1400 °C). Consequently, copper cannot be used to elaborate co-sintered metal/ceramic multilayer substrates unless some glass-forming compounds are added to the ceramic to lower the sintering temperature [1].

Using a sol–gel route for cordierite synthesis allows a drastic decrease of the sintering temperature without modifying the intrinsic properties of the ceramic [2]. Indeed, the sol–gel method allows mixing of the constituents on an atomic scale. Thus, interparticle diffusion during firing develops more quickly and at a lower temperature than in the classic method where mixing proceeds at the level of the grains.

In this way, copper-to-cordierite co-sintering was recently achieved and strong metal-to-ceramic bonding was obtained by an eutectic-bonding technique [3, 4]. Optimalized co-sintering conditions were determined and copper diffusion and the chemical composition at the interface of different co-sintered samples studied by various methods.

The present paper aims to give a more complete description of the chemical and structural characteristics of sol–gel processed cordierite before and after sintering. For this purpose, a set of complementary techniques were used: X-ray diffraction (XRD), scanning electron microscopy (SEM) and scanning transmission electron microscopy (STEM) both are associated with X-ray fluorescence (EDS-XRF), scanning electron-probe microanalysis (EPMA) and X-ray photoelectron spectroscopy (XPS).

2. Experimental procedure

2.1. Green- and sintered-cordierite processing

Several sol–gel preparation routes can be considered to elaborate cordierite, depending on the basic compounds used [5, 6]. Whereas alkoxides are essential to form the network of the gel, the other components can be introduced as soluble metal salts. Among the different combinations investigated, the method using a silicon-alkoxide precursor, with aluminium and magnesium introduced as nitrates, gave the best results on account of the physico-chemical properties of the ceramic and the cost of the process.

Fig. 1 presents a schematic diagram of this cordierite synthesis [6]. Silicon tetraethoxide, aluminium nitrate and magnesium nitrate were dissolved under vigorous stirring in a propanol–water mixture, giving rise to a stable solution. Adding ammonia induces hydrolysis and polycondensation, leading rapidly to a quite rigid gel. Solvents and residual nitrates were

0022–2461

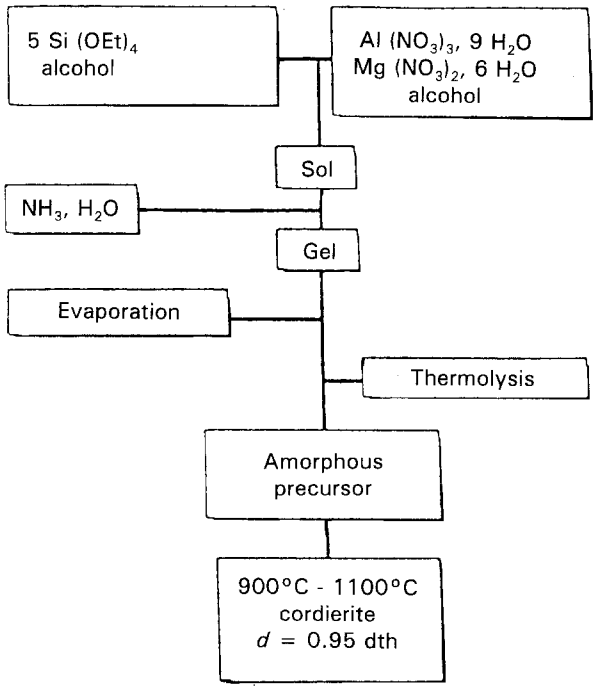

Figure 1 Flow chart for sol–gel synthesis of cordierite [6].

eliminated next by thermolysis at 250 °C and calcination at 700 °C. A more or less agglomerated amorphous white powder, which has the composition of cordierite, was obtained. Granulometry measurements give a mean diameter of 5 μm. SEM observations show that this value actually corresponds to the size of agglomerates, made up of particles of 0.01–0.1 μm in diameter as has been noted previously [6]. The specific area of the powder, measured by the Brunaver–Emmett–Teller (BET) method, is about 200 $m^2 g^{-1}$.

Uniaxially pressed (3000 $kg cm^{-2}$) green-cordierite pellets were next fired in an Ar/H_2O mixture and crystallization was followed by XRD. Sintering of the amorphous precursor started around 800 °C and crystallization into μ-cordierite, also called β-stuffed quartz (metastable hexagonal), began at about 850 °C. Conversion from μ-cordierite to α-cordierite called indialite (stable hexagonal) occurs rapidly in the range 1000–1100 °C. Thus, after a heating time of two hours at 1070 °C, XRD patterns on the final sintered material only reveal the presence of α-cordierite. The crystalline structure and thermal stability of these two forms of cordierite have already been described [7–9].

The following physical characteristics were measured on the sintered pellets: a linear shrinkage of 20–23% during firing, a final density of 95–98% of the theoretical value for indialite, a dielectric constant of ~ 4.5 at 1 MHz and a thermal expansion coefficient of $2 \times 10^{-6} °C^{-1}$.

2.2. Analytical methods

Apart from XRD, a set of complementary analytical methods were used to investigate, on a microscopic and on an atomic scale, the chemical and structural characteristics of the green- and sintered-cordierite elaborated. Except for STEM, all measurements were achieved on circular pellets (about 13 mm in diameter and 2 mm in thickness) obtained as mentioned above from a single preparation of the amorphous precursor.

SEM (Jeol JSM-840) associated with XRF was used to determine the morphology and the elemental composition of the surface of the cordierite pellets with a lateral resolution and an information depth of about 1 μm.

A scanning electron microprobe was used to determine the composition profiles across the polished section of a sintered pellet. Important surface roughness and macroporosity do not allow for this measurement on green samples.

XPS was used to investigate, on an atomic scale, the chemical composition of the outermost surface region. Lateral resolution is, however, very poor (~ 0.5 cm^2) and information is, consequently, averaged over this area. The XPS spectra were obtained with a VG ESCA 3 Mk-II apparatus using AlK_α radiation. Voltage calibration was achieved according to the NPL standard procedure [10]. The green and the sintered sample were analysed as-received and after a short argon-ion bombardment (to remove the surface contamination). Binding energies could thus be referenced with respect either to the C 1s line of hydrocarbon contamination (284.6 eV) or to the Ar 2p line of implanted argon (242.3 eV) to correct for the charge built up on these insulating sample surfaces during analysis [11]. Ion bombardment was carried out under mild conditions, i.e. ion energy 700 eV, current density 3 $\mu A cm^{-2}$, beam angle 45°.

Finally, STEM (Joel JEM-200CX) associated with XRF gave information about the morphology, elemental composition and crystalline structure of the sol–gel processed cordierite. Selected-area diffraction (SAD) patterns were indexed automatically using a computer program [12], with a data base containing all the oxides of the elements magnesium, aluminium and/or silicon listed in the updated JCPDS Powder Diffraction File. Samples were prepared from 100 μm thick cordierite wafers which were first abraded down to about 10 μm using a dimple grinder with 3 μm diamond powder and then thinned to perforation by argon-ion milling. Meaningful measurements could not be achieved on green cordierite since it crystallizes very rapidly under the electron beam. On the other hand, irradiation effects were only observed after a few hours for sintered samples.

3. Results

3.1. SEM and XRF

Fig. 2a and b, respectively, shows the aspect of the surface of a pressed green-cordierite pellet and of a sintered-cordierite pellet. Green cordierite is made up of small agglomerates, less than 1 μm in diameter. These agglomerates coalesce during sintering to form large smooth areas separated by cavities. As shown in Table I, EDS–XRF analyses over large areas (500×600 μm) give the same composition within measurement errors ($\pm$ 0.1–0.2 at %) for the green and for the sintered sample: there is no change of the overall composition during sintering. Departure from the theoretical composition is attributed to matrix

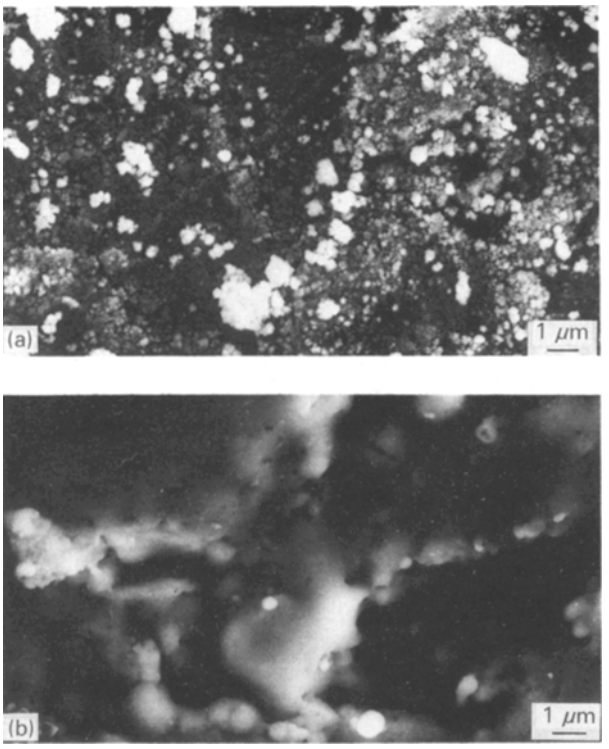

Figure 2 SEM micrographs of (a) green and (b) sintered sol–gel processed cordierite.

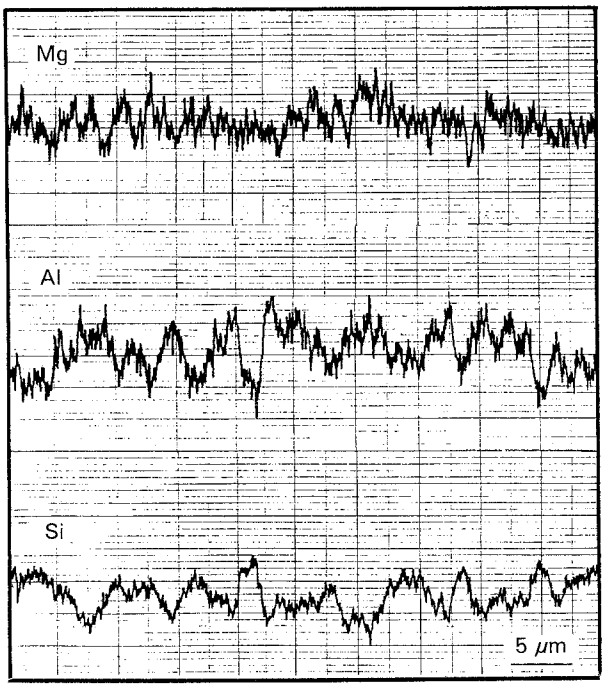

Figure 3 Mg, Al and Si concentration profiles obtained by scanning electron microprobe on a polished section of a sintered-cordierite sample.

TABLE I Elemental composition in at % obtained by EDS–XRF on green (G) and sintered (S) cordierite. For large areas (500 × 600 μm), scattering of the obtained values are within measurement errors (±0.1–0.2 at %). For small areas (1 × 1 μm), scattering range of measured concentration values for each element is given to show the importance of inhomogeneities

Theoretical		Large areas		Small areas	
		G	S	G	S
Al	13.8	15.2	14.9	14.5–15.3	12.0–15.9
Mg	6.9	6.8	6.6	6.8–8.2	3.9–10.6
Si	17.2	16.2	16.6	15.6–16.3	15.6–19.9
O	62.1	61.8	62.0	61.4–61.8	61.0–63.1

effects in quantitative XRF. They affect the concentration values, calculated by the ZAF correction method, through the atomic-number parameter Z and the absorption parameter A. The influence of the fluorescence parameter F is negligible in this case.

EDS–XRF analyses of small areas, a few micrometres in diameter, reveal composition inhomogeneities for the green and for the sintered material (Table I). For green cordierite, these inhomogeneities affect only a few areas and are characterized by a slight magnesium enrichment to the detriment of both aluminium and silicon. For sintered cordierite, they affect a much larger number of areas. The composition variations are also more important and concern all elements although magnesium shows the strongest deviation. In this case, there is no correlation between the variations of the different elements.

3.2. Scanning electron microprobe

Magnesium, aluminium and silicon profiles measured through the polished section of a sintered sample are given in Fig. 3. Since there is little correlation between the three elemental profiles, the observed features cannot be related to topographic effects but correspond to weak composition fluctuations. However, no systematic trend is found between any two of these elements. Thus, though the material shows some heterogeneities, there is no evidence for the presence of precipitates of compounds with different stoichiometry, at least within the resolution of the experiment (~1 μm).

3.3. X-ray photoelectron spectroscopy

Fig. 4 shows an overall XPS spectrum obtained on the as-received sintered-cordierite sample. On such spectra, line identification readily allows an elemental characterization of the surface. The energy and shape of the photoelectron and Auger peaks give information about the chemical-bonding state of the different elements. Finally, relative surface concentrations are determined by peak-area measurements using tabulated sensitivity factors [13].

Table II lists the binding (kinetic) energy of the main photoelectron (Auger) lines as well as the magnesium and the oxygen Auger parameters [14, 15] measured on the green and on the sintered sample. The values obtained are, within measurement errors (± 0.1–0.2 eV), the same for the two samples, before and after removal of the hydrocarbon contamination. Peak-shape analysis shows that only one bonding state is present for each element on the two samples.

The Al 2p, Si 2p and O 1s binding energies are in general agreement with the values reported for a number of alumino-silicates [15]. Moreover, our oxygen Auger parameter and O 1s–Si 2p line-energy difference are within the range of the values found for these compounds. The chemical shift of the Mg 2p and

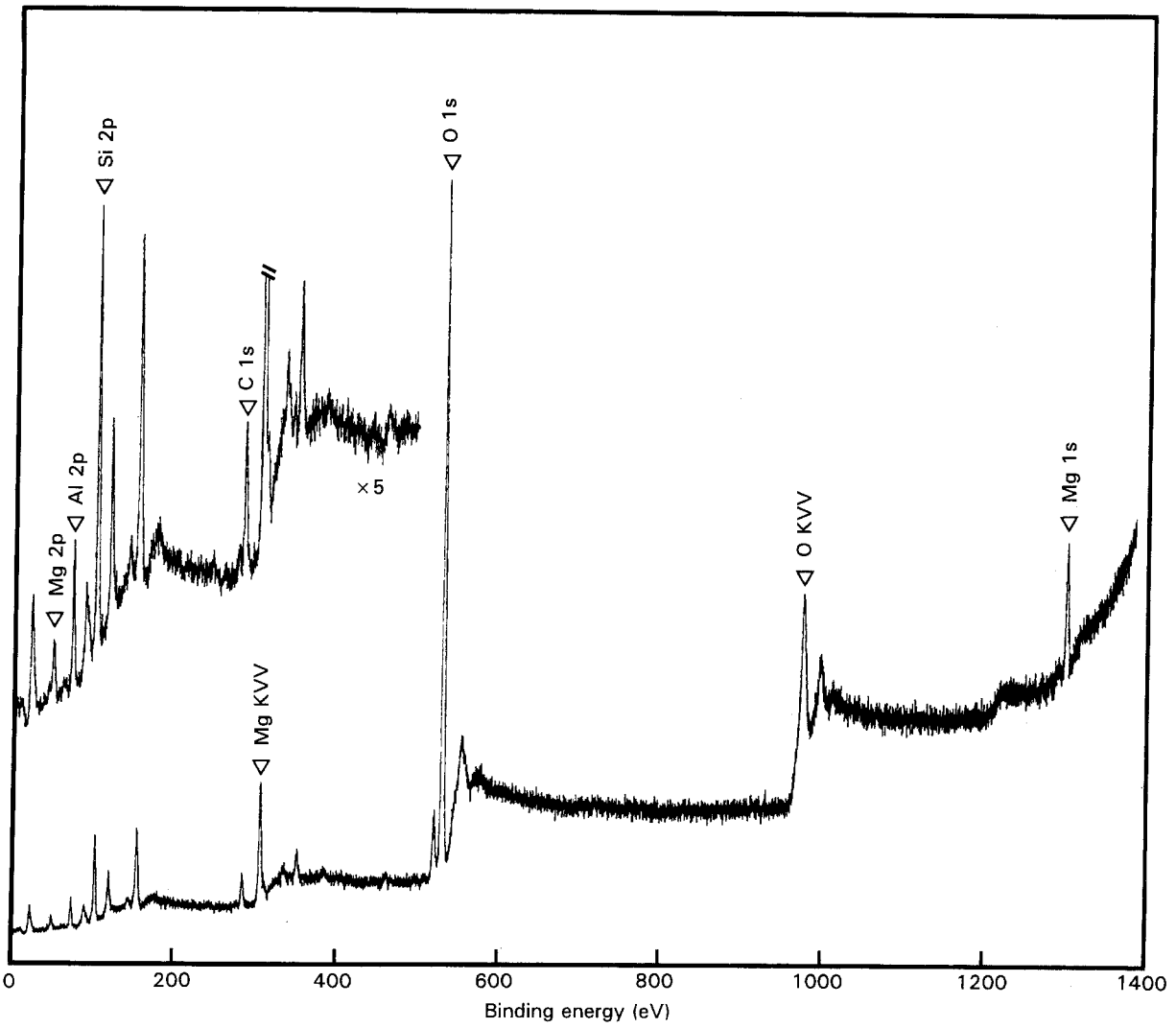

Figure 4 X-ray photoelectron spectrum of sintered as-received cordierite. The C 1s peak is due to hydrocarbon contamination on the surface of the sample.

TABLE II Photoelectron binding energy, E_B, Auger kinetic energy, E_K, and Auger parameter, α, measured on green and sintered cordierite. E_B and E_K are Fermi-level referenced. The estimated error is 0.1–0.2 eV

	E_B (eV)	E_K (eV)	α (eV)
Al 2p	74.8		
Mg 2p	51.1	MgKVV 1179.4	1230.5
Mg 1s	1304.1		2483.7
Si 2p	102.9		
O 1s	532.0	OKVV 507.9	1039.9

Mg 1s peaks as well as the magnesium Auger parameters indicate that magnesium is bound to oxygen too [13, 14]. Although no further conclusion can be drawn from the binding-energy analysis, these results are in agreement with the cordierite structure where SiO_4 and AlO_4 tetrahedra form the network and magnesium atoms as *gegen* ions occupy oxygen-based octahedral sites. Only one reference reporting XPS data of cordierite could be found in the literature [16]. The data reported there (Mg 2p 51.7 eV, Al 2p 75.4 eV, Si 2p 103.8 eV) are markedly higher than our results. The O 1s binding energy is not given. Taking our O 1s–Si 2p value of 429.1 eV leads to an O 1s binding energy of 532.9 eV which is out of the range of values generally observed for oxides. So we think that their values are shifted by about 0.7 eV to higher energies due to inaccurate energy-scale referencing.

For both samples, quantitative analysis gives similar results before and after removal of the surface contamination. For the green sample, we obtain a 14.1 at % Al, 6.1 at % Mg, 17.5 at % Si, 62.3 at % O composition in good agreement with the bulk composition (13.8 at % Al, 6.9 at % Mg, 17.2 at % Si, 62.1 at % O) considering a 10% relative measurement error. A constant in-depth composition can therefore be expected. Unlike the green sample, the sintered sample gives a surface composition which is slightly but significantly different from the bulk: 11.0 at % Al, 4.0 at % Mg, 21.5 at % Si, 63.5 at % O. Sputter depth profiling down to a few tens of nanometres shows no departure from this composition.

3.4. STEM and XRF

The bright-field image in Fig. 5 shows a representative area of the morphology of a sol–gel processed sintered-cordierite sample. Note the presence of many well-shaped particles ranging from about 20 to 200 nm. EDS–XRF microanalyses of areas 0.3 to 2.0 μm in

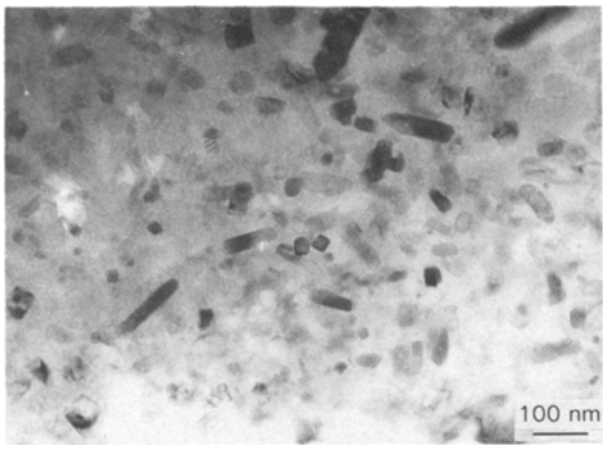

Figure 5 Bright-field transmission electron micrograph of a sol–gel processed sintered-cordierite sample.

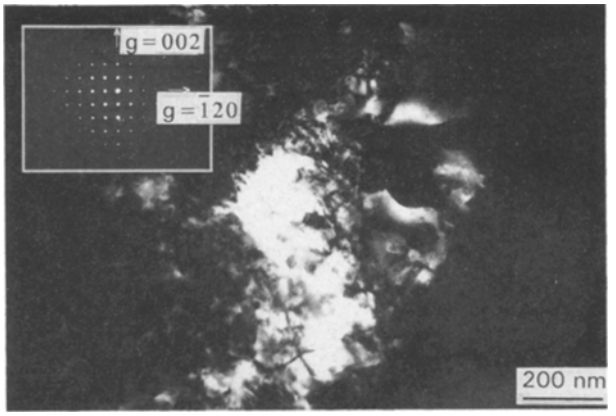

Figure 6 Dark-field image produced with the $\bar{1}\,2\,0$ spot of the inset SAD pattern. This pattern shows reflections from α-cordierite ([2 1 0]-zone-axis pattern) formed from an area 0.3 μm in diameter.

diameter give composition variations within the range found by this method in SEM on small areas (see Table I). As in that case, magnesium shows the strongest deviation and there is no correlation between the variations of the different elements. SAD on areas about 0.3 μm in diameter leads to different images: either ring patterns or spot patterns or a combination of both depending on the location. The results obtained on the cordierite matrix and on precipitates with different elemental composition will be presented separately hereafter.

SAD spot patterns corresponding to the cordierite matrix can be obtained easily although they are formed from areas containing a great number of small-size particles. Since most patterns can be indexed according both to α-cordierite (hexagonal) and β-cordierite (orthorhombic), we analysed spot intensities and series of patterns obtained by tilting the sample in order to identify the cordierite phase. Actually only α-cordierite was found. Fig. 6 shows a dark-field image produced with the $\bar{1}\,2\,0$ spot of the SAD pattern shown in the inset. The pattern shows reflections from α-cordierite aligned along the [2 1 0]-zone axis. Note that a large area composed of many particles forms this spot. Fig. 7 shows a high-resolution image of a similar area, with lattice fringes corresponding to (1 0 0) planes. Observe the presence of many grains surrounded by an amorphous phase. The aligned crystallographic orientation of the different grains is explained by slicing through a complex-shaped particle when preparing the sample. This kind of particle shape is actually expected to develop by coalescence of individual grains during sintering. Lattice spacing was generally within measurement error ($\pm$ 0.006 nm), in agreement with the expected value for α-cordierite. However, careful analysis of some lattice images showed deviations of the lattice parameters of more than 1% with respect to those given in the Powder Diffraction File, i.e. 0.977 nm for *a* and 0.935 nm for *c*. These variations cannot be attributed to inaccurate calibration of the camera length since they were measured on the same image in some cases. They cannot be interpreted by thickness variations either, since they were measured in the centre of the grains [17].

The average thickness of the amorphous phase surrounding the cordierite grains is about 20–30 nm. Analysis of cross-sectional samples show that this amorphous phase is present at the outermost surface too with a comparable thickness. No accurate EDS–XRF measurement could be achieved on this phase due to its small size. However, no major composition difference with respect to cordierite is expected, as compared to the precipitates. Finally, diffraction patterns and lattice images were also checked for the presence of μ-cordierite but no evidence was found for the presence of this compound.

Two kinds of precipitates were observed in the cordierite sample: many small precipitates, a few tens of nanometres in size, located among the cordierite particles and some large precipitates, a few hundreds of nanometres in size, well separated from them. Fig. 8 shows a diffraction image taken on the cordierite matrix over a 0.3 μm area. Apart from different diffraction spots of cordierite, careful analysis of the diffraction rings clearly indicate the presence of spinel ($MgO{\cdot}Al_2O_3$) and mullite ($3Al_2O_3{\cdot}2SiO_2$). A few minor rings could not be interpreted, however. These compounds are present as numerous small crystals among the large cordierite particles. This is illustrated in Fig. 9 which represents a dark-field image of the cordierite matrix obtained with part of the diffraction diagram, as shown in Fig. 8. The bright particles can be attributed to mullite crystals. Actually, in Fig. 7, (1 1 1) lattice fringes of a spinel crystal can be noted in the upper part of the image (enlarged view in the inset). The presence of these small precipitates explains the composition variations observed for the cordierite matrix. Some large precipitates appear in rather featureless areas without any cordierite particles (Fig. 10). Their identification using either ring or spot diffraction patterns was unsuccessful, due respectively, to the small number of precipitates or to their small size. More specific studies using convergent-beam microdiffraction techniques have started to go further into this problem. To get some idea about the chemical composition of these precipitates and their surrounding phase, we carried out a number of EDS–XRF measurements with a 60 nm beam diameter. With

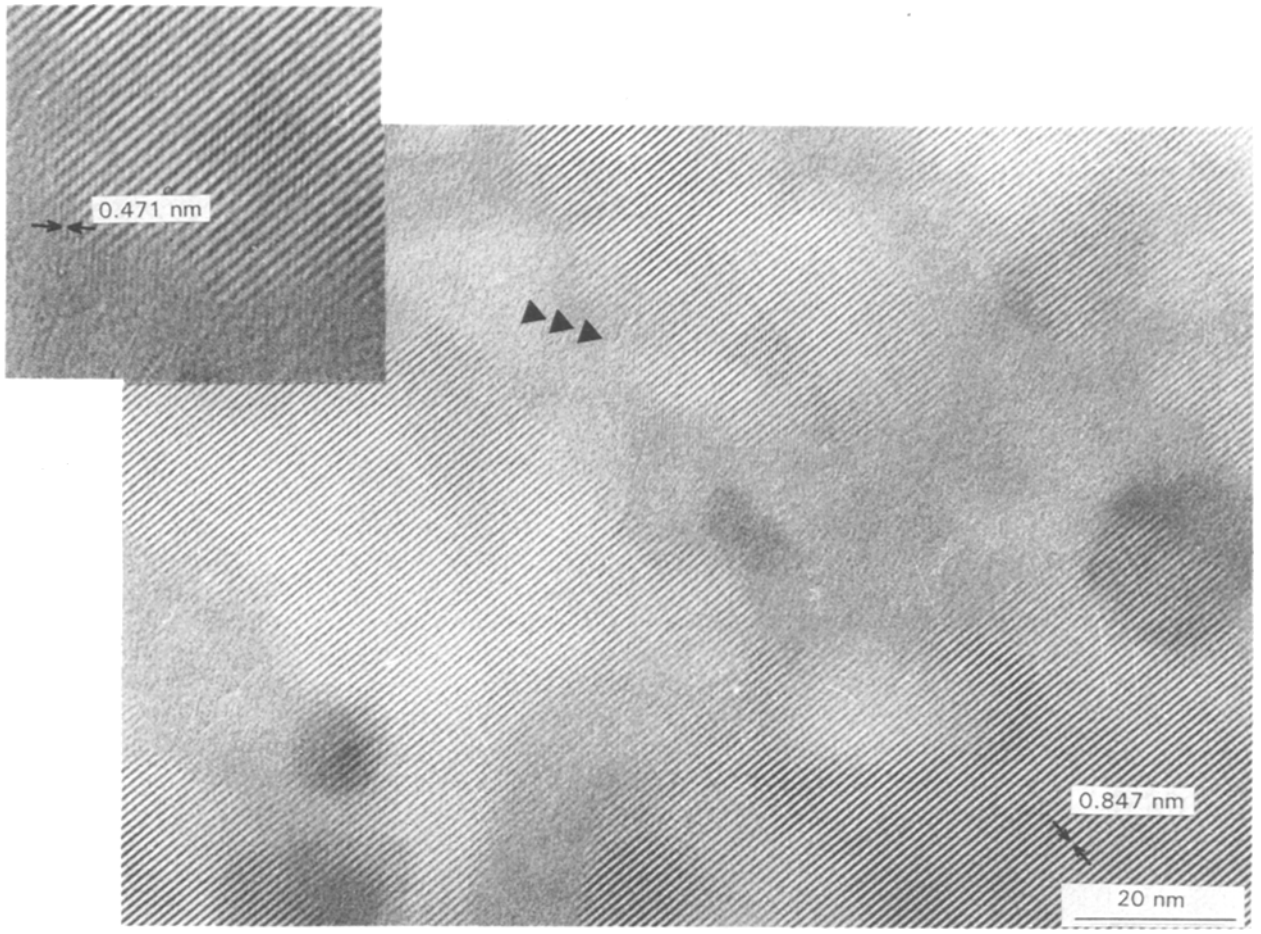

Figure 7 Lattice-fringe image with fringes corresponding to the (1 0 0) planes of α-cordierite. The inset is an enlarged view showing the (1 1 1) lattice fringes of a small spinel crystal.

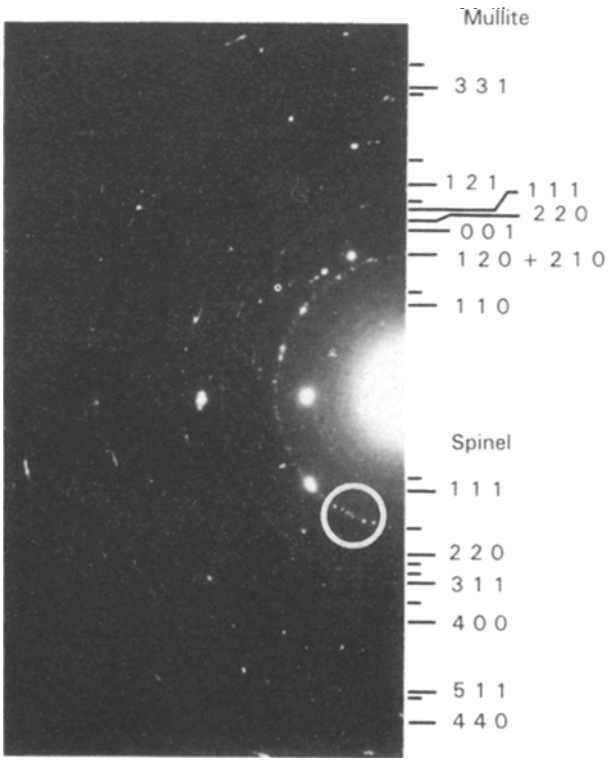

Figure 8 Diffraction image obtained on the cordierite matrix on a 0.3 μm area. Bright spots correspond to α-cordierite reflections. Diffraction rings are indexed with larger bars for mullite in the upper part and with larger bars for spinel in the lower part of the figure. The white circle represents the aperture used to produce the dark-field image of Fig. 9.

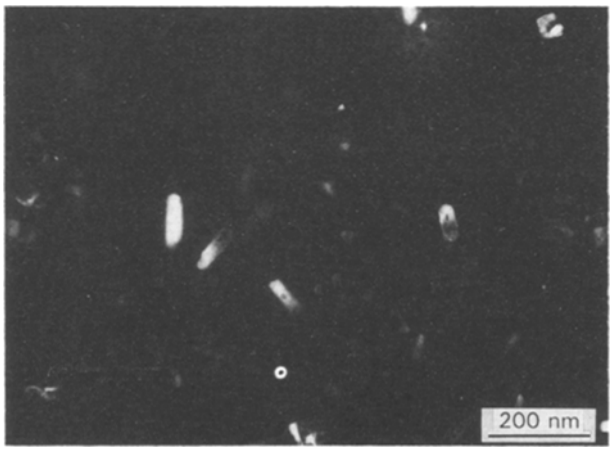

Figure 9 Dark-field image obtained with the aperture represented in the diffraction image of Fig. 8. Bright particles are identified as mullite crystals.

respect to cordierite, drastic changes in the magnesium concentration were observed: the precipitates showed a high magnesium concentration (about 14 at %) whereas the surrounding phase was magnesium depleted (about 3 at %). In both cases, we generally observed a significant silicon enrichment with respect to aluminium: the Al/Si ratio varied in the range 0.5–0.9 compared to 0.80 for α-cordierite (Fig. 11). From the composition measured on these large precipitates, we would thus expect the presence of compounds such as pyrope ($3MgO{\cdot}Al_2O_3{\cdot}3SiO_2$) or enstatite ($MgO{\cdot}SiO_2$).

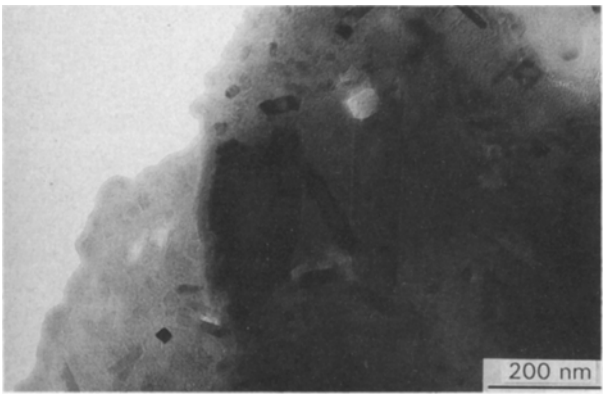

Figure 10 Bright-field transmission electron micrograph of an area with large precipitates. Note the featureless area surrounding the precipitates.

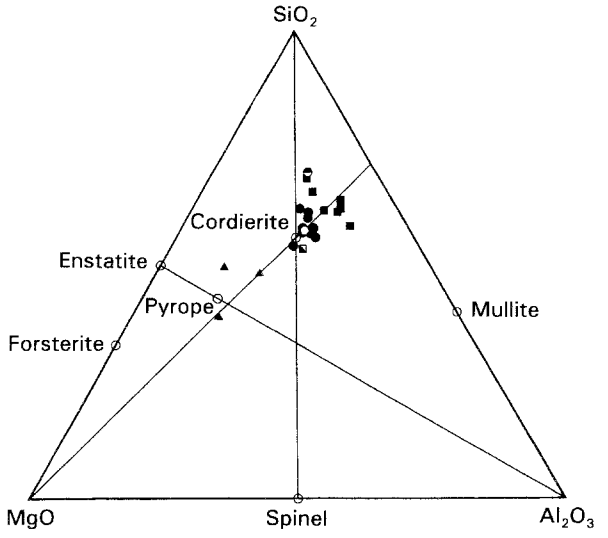

Figure 11 $MgO-Al_2O_3-SiO_2$ composition diagram with concentrations measured by different methods on green and sintered cordierite: (○) stoichiometric composition, (◯) green (XPS), (⬟) sintered (XPS), (◣) green/sintered (XRF on large areas), (●) sintered (XRF microanalysis on cordierite matrix), (■) sintered (XRF microanalysis on amorphous areas), and (▲) sintered (XRF microanalysis on large precipitates).

4. Discussion and conclusion

Many authors have already pointed out the importance of the various synthesis parameters on the homogeneity of the resultant cordierite gel [5, 6, 18–22]. The nature of the solvents, amount of water, type and dilution of the catalyst, addition rates and reaction temperature are known to strongly influence the gel homogeneity through the hydrolysis and polymerization mechanisms. However, a general forecasting of the nature and the amount of heterogeneities is not straightforward. A systematic study of the processing parameters [6] allowed us to determine optimalized conditions which lead to a sintered material very close to pure α-cordierite, at least according to macroscopic characterization methods such as XRD or XRF over large areas. But, at a smaller scale, the present study shows a slightly different picture. For the sake of clarity, we will discuss the results on the cordierite matrix and on the precipitates separately.

The sintered-cordierite sample presents many well-shaped grains, identified as α-cordierite, with a size ranging from about 20 to 200 nm. This size can be correlated with the size of the particles of the green powder, ranging from about 10 to 100 nm. These amorphous particles start to coalesce above 800 °C from a viscous-flow mechanism, leading to complex-shaped grains. Crystallization into μ-cordierite starts at about 850 °C but this compound is not detected in our final sintered material. It is indeed expected to transform rapidly into α-cordierite in the range 970 to 1050 °C, as pointed out by Broudic *et al.* [22]. Thus, after heating for 2 h at 1070 °C, we obtained large areas of coalesced α-cordierite grains with aligned crystallographic orientations, surrounded by an amorphous phase which is present at the surface too. Chemical analyses of this phase by XRF and XPS indicated appreciable magnesium depletion and an increased Si/Al ratio with respect to α-cordierite, characteristic of a vitreous phase. Further heating at higher temperatures would allow crystallization to progress by direct transformation of this remaining amorphous phase into α-cordierite [22]. The observed deviations of the lattice parameters from the expected values for α-cordierite are probably explained by the presence of tiny perturbed domains characterized either by some departure from stoichiometry or by some local Si, Al ordering [23, 24]. Replacement of Si by Al in MO_4 tetrahedra, or vice versa, indeed leads to slight changes of the lattice parameters due to different M–O bond lengths [25]. Si, Al ordering also influences the lattice parameters through distortion of the MO_4 tetrahedra and consequent distortion of the structure.

The presence of precipitates of different chemical composition in the sintered cordierite sample shows that some demixing occurs in our material. However a question remains as to whether these heterogeneities are due to inhomogeneities in the initial xerogel or not. XRF measurements reveal that a few local heterogeneities already exist in the green-cordierite sample. These inhomogeneities are characterized by an important magnesium enrichment whereas the Al/Si ratio remains nearly equal to the α-cordierite value. The composition and the distribution of these inhomogeneities can be correlated with those of the large precipitates observed by TEM on the sintered sample. These large precipitates would thus be a result of the observed inhomogeneities which pre-exist in the gel. On the other hand, no areas with compensating magnesium depletion are observed on the green material. This depletion is either distributed uniformly over the whole material or the size of corresponding areas are beyond the resolution of the analytical methods used. Finally, in the sintered sample, we observe many small precipitates, a few tens of nanometres in size, which we identify as small spinel and mullite crystals. However, we did not observe any precursor of these small crystals in the green powder.

Further studies [26, 27] using in particular high-resolution TEM and convergent-beam techniques are already well in progress to investigate in more detail the results presented here. They allow confirmation of

the determining role of the gel inhomogeneity in the formation of precipitates and give some information about the demixing mechanisms. They also make precise the role and thermal stability of the μ-cordierite and the amorphous cordierite, and they throw some light on the α–β phase transformation.

Acknowledgements

We are very grateful to B. S. Han and J. Faerber for their expert technical assistance.

References

1. A. H. KUMAR, P. W. McMILLAN and R. R. TUMMALA, US Patent 4413061 (1983).
2. J. C. BERNIER, P. POIX, J. L. REHSPRINGER, G. VILMIN and S. VILMINOT, French Patent 85-10873 (1985).
3. V. OLIVER-BROUDIC, J. GUILLE, J. C. BERNIER, B. S. HAN, J. WERCKMANN, J. FAERBER, P. HUMBERT and B. CARRIERE, *Mater. Sci. Engng. A* **109** (1989) 77.
4. J. WERCKMANN, B. S. HAN, J. FAERBER, P. HUMBERT, B. CARRIERE, C. ESNOUF, N. CHARDON, J. GUILLE and J. C. BERNIER, *Mat. Res. Soc. Symp. Proc.* **153** (1989) 403.
5. J. C. BERNIER, J. L. REHSPRINGER, S. VILMINOT and P. POIX, *Mat. Res. Soc. Symp. Proc.* **73** (1986) 129.
6. J. C. BROUDIC, S. VILMINOT and J. C. BERNIER, *Mater. Sci. Engng. A* **109** (1989) 253.
7. M. D. KARKHANAVALA and F. A. HUMMEL, *J. Amer. Ceram. Soc.* **36** (1953) 389.
8. K. LANGER and W. SCHREYER, *Amer. Mineral.* **54** (1969) 1442.
9. P. PREDECKI, J. HAAS, J. FABER Jr. and R. L. HITTERMAN, *J. Amer. Ceram. Soc.* **70** (1987) 175.
10. M. T. ANTHONY and M. P. SEAH, *Surf. Interface Anal.* **6** (1984) 95, 107.
11. S. KOHIKI, T. OHMURA and K. KUSAO, *J. Electron Spectrosc. Relat. Phenom.* **28** (1983) 229.
12. P. A. STADELMANN, *Ultramicroscopy* **21** (1987) 131.
13. C. D. WAGNER, W. M. RIGGS, L. E. DAVIS, J. F. MOULDER and G. E. MUILENBERG, edited by G. E. Muilenberg "Handbook of X-ray photoelectron spectroscopy," (Perkin-Elmer Corporation, Eden Prairie MI, 1979).
14. C. D. WAGNER, *Faraday Discuss. Chem. Soc.* **60** (1975) 291.
15. C. D. WAGNER, D. E. PASSOJA, H. F. HILLERY. T. G. KINISKY, H. A. SIX, W. T. JANSEN and J. A. TAYLOR, *J. Vac. Sci. Technol.* **21** (1982) 933.
16. M. BORTZ and F. S. OHUCHI, *J. Appl. Phys.* **64** (1988) 2054.
17. P. B. HIRSCH, A. HOWIE. R. B. NICHOLSON, D. W. PASHLEY and M. J. WHELAN, "Electron microscopy of thin crystals" (Butterworths, London, 1965) p. 161.
18. B. E. YOLDAS, *J. Mater. Sci.* **14** (1979) 1843.
19. T. HAYASHI, T. YAMADA and H. SAITO, *J. Mater. Sci.* **18** (1983) 3137.
20. C. GENSSE and U. CHOWDERY, *Mat. Res. Soc. Symp. Proc.* **72** (1986) 297.
21. H. SUZUKI, K. OTA and H. SAITO, *Yogyo Kyokai Shi* **95** (1987) 25.
22. J. C. BROUDIC, J. GUILLE and S. VILMINOT, in Proceedings of the 1st Conference of the European Ceramic Society, Maastricht, The Netherlands, June 1989.
23. T. ARMBRUSTER, *N. Jb. Miner. Mh.* **6** (1985) 255.
24. C. A. FYFE, G. C. GOBBI and A. PUTNIS, *J. Amer. Chem. Soc.* **108** (1986) 3218.
25. G. V. GIBBS, *Amer. Mineral.* **51** (1966) 1068.
26. L. EL CHAHAL. J. WERCKMANN, G. EHRET, G. POURROY, T. EPICIER and C. ESNOUF, in Proceedings of the 2nd Conference of the European Ceramic Society, Augsburg, FRG, September 1991.
27. L. EL CHAHAL. J. WERCKMANN, G. EHRET. G. POURROY, C. ESNOUF and T. EPICIER, to be published.

Received 13 March 1992
and accepted 11 January 1993